Thermal lattice Boltzmann simulations of variable Prandtl number turbulent flows

Min Soe and George Vahala
Department of Physics, College of William & Mary, Williamsburg, Virginia 23187

Pavol Pavlo
Institute of Plasma Physics, Czech Academy of Sciences, Praha 8, Czech Republic

Linda Vahala
Department of Electrical and Computer Engineering, Old Dominion University, Norfolk, Virginia 23529

Hudong Chen
Exa Corporation, Cambridge, Massachusetts 02139

(Received 9 June 1997; revised manuscript received 24 October 1997)

Thermal lattice Boltzmann (TLBE) models that utilize the single relaxation time scalar Bhatnagar, Gross, and Krook collision operator have an invariant Prandtl number. For flows with arbitrary Prandtl number, a matrix collision operator is introduced. The relaxation parameters are generalized so that the transport coefficients become density independent. TLBE simulations are presented for two-dimensional free decaying turbulence induced by a strongly perturbed double velocity shear layer for various Prandtl numbers. [S1063-651X(98)08304-4]

PACS number(s): 47.11.+j, 47.27.−i

I. INTRODUCTION

The lattice Boltzmann method (LBE), an outgrowth of lattice gas automaton (LGA) [1–3], has been considered recently as a possible alternative explicit numerical scheme to conventional methods for solving nonlinear macroscopic physical systems, in particular for Navier-Stokes flows. Like LGA, LBE is ideally suited for parallel computing environment while in some respects improving the ancestral LGA model by eliminating statistical noise, non-Galilean invariance as well as pressure that is velocity dependent. This is accomplished essentially in LBE at the expense of working with floating point rather than Boolean variables and the need to specify an appropriate equilibrium distribution to which collisions drive the macroscopic system. The price paid for this generalization is the loss of an H theorem and possible numerical instabilities. The physical interpretation of LBE consists of two steps: (1) a streaming step that advects particles from a particular node to its nearest neighbor according to their lattice velocities, and (2) a collision step that describes the local change in the distribution function due to particle collisions at each nodal site. The inherent beauty of the method is that both operations are local and this makes LBE ideal for multiparallel processor machines. Of course there are many kinetic models that will reproduce the desired form of macroscopic nonlinear transport equations. In LBE, one goes from a macroscopic to a microscopic description to work with the simplest possible micromodel, which is computationally most efficient. Its motivations rest on the fact that the details of the microscopic dynamics affect only the transport coefficients and do not alter the form of fluid conservation equations.

An important refinement of the LBE was proposed in Refs. [4,5], where the collision operator was generically linearized for simplicity as a product of the collision matrix and the perturbative part of the particle distribution function. Even further simplification was proposed by introducing its Bhatnagar, Gross, and Krook (BGK) version [6] in which the collision operator is condensed into a single relaxation parameter. This scalar collision operator is found not only sufficient to be able to recover the desired nonlinear transport equations under Chapman-Enskog expansions, but is computationally more efficient. Even though the dynamical phase space has been increased by going from macroscopic to a microscopic description, the advantages of explicit lattice BGK models [6–9] can be summarized as follows: parallelism of the method, the simplicity of the code, easy treatment of realistic boundary conditions, and ready extension to 3D problems. However, most of the thermal lattice Boltzmann models (TLBE) that utilize the BGK collision operator [9–11], utilize only one relaxation time scale so that both the shear viscosity μ and the thermal conductivity κ transport coefficients are intrinsically linked. Therefore these models allow only for fixed Prandtl number flows, where $\mathrm{Pr}=\mu/\kappa$. It is well known that, under appropriate conditions, the heat flux to walls can be a function of the Prandtl number: for some range of Prandtl number, the heat flux is from the walls, while in other Prandtl number ranges, the heat flux is into the walls and hence there is interest in observing the change in flow characteristics with Prandtl number. Here we extend TLBE to handle flows with variable Prandtl numbers. We shall comment on earlier variable Prandtl number attempts made by other authors [12,13] in Sec. V.

In the following section, we will describe an extended tensor collision operator [14] that allows variable Prandtl number flows. Incorporation of an additional free parameter in the off-diagonal components of the matrix collision operator will lead to a multirelaxation scheme. The relaxation parameters will be generalized so that transport coefficients become density independent, a result well known from classical kinetic theory of dilute gases [15]. All previous lattice Boltzmann models have suffered from the problem of

density-dependent transport coefficients. Even though this poses no problem for incompressible flows, it is critical and must be handled for compressible fluid simulations. In Sec. II, we discuss the Chapman-Enskog procedure used in LBE and derive the desired macroscopic fluid equations and transport coefficients. In Sec. III, we present TLBE simulation results for the effect of velocity shear layer on a heat front for various Prandtl numbers. The numerical stability of the proposed model is discussed in Sec. IV, while Sec. V is devoted to a summary and concluding remarks. In the Appendix, we perform numerical tests to verify that our extended tensor collision operator (introduced in Sec. II) can be properly used for variable Prandtl number flows.

II. TLBE WITH EXTENDED COLLISION OPERATOR

The governing equation of TLBE, which in local microscopic units of length and time takes the generic form

$$N_{pi}(\mathbf{x}+\mathbf{e}_{pi},t+1)-N_{pi}(\mathbf{x},t)=\Delta_{pi}, \quad i=1,...,b_p. \tag{1}$$

This describes the evolution of the mean particle population N_{pi} in the discrete phase space. The indices p and i are for sublattice and lattice links, respectively. Thus, for a 2D hexagonal lattice, $b_p=6$ as each lattice node is connected to 6 other spatial sites. Strictly speaking, one should call this a triangular lattice. A hexagonal lattice has only 3 links. $\mathbf{e}_{pi}$ is the lattice vector giving the velocity of moving particles in the system. The speed in each sublattice is $|\mathbf{e}_{pi}|=p$. To recover the correct macroscopic behavior, rest particles must also be included and will be labeled by $p=0$ with $\mathbf{e}_0=0$ and $b_0=1$. Δ_{pi} is the collision matrix whose eigenvalues control the transport coefficients. In nearly all lattice Boltzmann literature, Δ_{pi} has been reduced to the BGK [6] form for computational simplicity,

$$\Delta_{pi}=-\frac{1}{\tau}(N_{pi}-N_{pi}^{\mathrm{eq}}). \tag{2}$$

where τ is a relaxation parameter that determines the time for N_{pi} to relax to some appropriately chosen equilibrium distribution function N_{pi}^{eq}. Unfortunately, this yields an invariant Prandtl number. This is because the scalar collision operator in BGK takes the form $-(1/\tau)\delta_{ij}(N_{pj}-N_{pj}^{\mathrm{eq}})$ and this forces the eigenvalues for the momentum and energy transport modes to be identical because of the Kronecker tensor δ_{ij}. Thus for variable Prandtl number flows, it is convenient to generalize the scalar collision operator into a circulant matrix with the inclusion of another free parameter θ in the off diagonal components [14]

$$\Delta_{pi}=-\frac{1}{\tau}(N_{pi}-N_{pi}^{\mathrm{eq}})-\frac{\theta}{b_p e_p^2}\sum_j e_{pi\alpha}e_{pj\alpha}(N_{pj}-N_{pj}^{\mathrm{eq}})$$

$$\equiv\frac{-1}{\tau}\sum_j A_{ij}(N_{pj}-N_{pj}^{\mathrm{eq}}). \tag{3}$$

Here we do not define Δ_{pi} by the scattering rules as in LGA, but enforce certain symmetry requirements. As a result, A_{ij} is symmetric, cyclic, with the nonzero eigenvalues

$$\lambda_1=1, \tag{4}$$

$$\lambda_2=\left(1+\frac{\theta_\tau}{2}\right) \tag{5}$$

of multiplicity 4 and 2, respectively, for a hexagonal lattice. The equilibrium distribution N_{pi}^{eq} is assumed to be a truncated power series [9] in the mean velocity $\mathbf{v}$:

$$N_{pi}^{\mathrm{eq}}=A_p+B_p(\mathbf{e}_{pi}\cdot\mathbf{v})+C_p(\mathbf{e}_{pi}\cdot\mathbf{v})^2+D_p\mathbf{v}^2+E_p(\mathbf{e}_{pi}\cdot\mathbf{v})^3$$
$$+F_p(\mathbf{e}_{pi}\cdot\mathbf{v})\mathbf{v}^2. \tag{6}$$

The coefficients $A_p, B_p \cdots F_p$ are functions of the mean density n and mean temperature ε, where

$$n=\sum_{pi} N_{pi}, \tag{7}$$

$$n\mathbf{v}=\sum_{pi} N_{pi}\mathbf{e}_{pi}, \tag{8}$$

$$n\varepsilon=\frac{1}{2}\sum_{pi} N_{pi}(\mathbf{e}_{pi}-\mathbf{v})^2. \tag{9}$$

The explicit form of these coefficients depends on the geometry of the underlying lattice and are given in Ref. [9] for a 2D hexagonal lattice. Constraints imposed on N^{eq} and the collision matrix Δ_{pi} are such that the local collisional invariants $\Sigma_{pi}\Delta_{pi}=0$, $\Sigma_{pi}\Delta_{pi}\mathbf{e}_{pi}=0$, and $\Sigma_{pi}\Delta_{pi}\mathbf{e}_{pi}^2=0$ are satisfied. Further physical constraints are also imposed: in particular, one must impose Galilean invariance and require that the pressure be independent of the mean macroscopic velocity.

To recover the desired thermal Navier-Stokes equations, we first translate the discrete lattice Boltzmann equation into the continuous space and time form by Taylor expanding (1) in the long wavelength and the low frequency limit:

$$\partial_t N_{pi}+e_{pi\alpha}\partial N_{pi}+\frac{1}{2}\partial_t^2 N_{pi}+e_{pi\alpha}\partial_\alpha\partial_t N_{pi}$$

$$+\frac{1}{2}e_{pi\alpha}e_{pi\beta}\partial_\alpha\partial_\beta N_{pi}=\Delta_{pi}(N), \tag{10}$$

where the subindices α and β represent Cartesian components with summation over repeated subscripts. We now utilize the Chapman-Enskog procedure, assuming the following multiscale expansion for the time and spatial derivatives in a small quantity ϵ:

$$\partial_t\rightarrow\epsilon\partial_{t1}+\epsilon^2\partial_{t2}, \quad \partial_\alpha\rightarrow\epsilon\partial_\alpha. \tag{11}$$

ϵ is, in essence, the Knudsen number. We also expand the distribution function as

$$N_{pi}=N_{pi}^{(0)}+\epsilon N_{pi}^{(1)} \tag{12}$$

with $N_{pi}^{(0)}=N_{pi}^{\mathrm{eq}}$, and $N_{pi}^{(1)}$ is the perturbative part of the distribution function. Substituting the above expressions into Eq. (10), we obtain

$$O(\epsilon): \quad (\partial_{t1}+e_{pi\alpha}\partial_\alpha)N_{pi}^{(\mathrm{eq})}=-\frac{1}{\tau}\sum_j A_{ij}N_{pj}^{(1)}, \tag{13}$$

$$O(\epsilon^2): \quad \partial_{t2} N_{pi}^{\mathrm{eq}} + (\partial_{t1} + e_{pi\alpha}\partial_\alpha) N_{pi}^{(1)} + \tfrac{1}{2}(\partial_{t1} + e_{pi\alpha}\partial_\alpha)^2 N_{pi}^{\mathrm{eq}} = 0. \tag{14}$$

Taking moments of Eq. (13) yields

$$\partial_{t1} n + \partial_\alpha (n v_\alpha) = 0, \tag{15}$$

$$\partial_{t1} (n v_\alpha) + \partial_\beta \Pi_{\alpha\beta}^{\mathrm{eq}} = 0, \tag{16}$$

$$\partial_{t1} (n\varepsilon + \tfrac{1}{2} n v^2) + \partial_\alpha Q_\alpha^{\mathrm{eq}} = 0 \tag{17}$$

with momentum and heat fluxes

$$\Pi_{\alpha\beta}^{\mathrm{eq}} = \sum_{pi} e_{pi\alpha} e_{pi\beta} N_{pi}^{\mathrm{eq}}, \tag{18}$$

$$Q_\alpha^{\mathrm{eq}} = \frac{1}{2} \sum_{pi} \mathbf{e}_{pi}^2 e_{pi\alpha} N_{pi}^{\mathrm{eq}}. \tag{19}$$

Note that the right-hand side of Eq. (13) does not contribute to the moment equations (15)–(17). This is because of the constraints imposed for the local collisional invariants. By making use of Eq. (6) we can write Eqs. (18) and (19) in terms of macroscopic quantities:

$$\Pi_{\alpha\beta}^{\mathrm{eq}} = \frac{2}{D} n\varepsilon \delta_{\alpha\beta} + n v_\alpha v_\beta, \tag{20}$$

$$Q_\alpha^{\mathrm{eq}} = \frac{D+2}{2} n\epsilon v_\alpha + \frac{1}{2} n v^2 v_\alpha, \tag{21}$$

where D is the dimension of the lattice. Thus by substituting these expressions into Eqs. (16) and (17), we find the following nondissipative Euler fluid equations, i.e., at $O(\epsilon)$:

$$\partial_{t1} n + \partial_\alpha (n v_\alpha) = 0, \tag{22}$$

$$\partial_{t1} (n v_\alpha) + \partial_\beta (n v_\alpha v_\beta) = -\partial_\alpha P, \tag{23}$$

$$\partial_{t1} (n\varepsilon) + \partial_\alpha (n\varepsilon v_\alpha) = -P \partial_\alpha v_\alpha. \tag{24}$$

Here we can identify the velocity-independent portion of the momentum flux tensor in Eq. (20) as the pressure P, with $P = n\varepsilon$; i.e., we find the equation of state for an ideal gas.

To obtain the continuity, momentum, and energy equations at $O(\epsilon^2)$, we take appropriate moments of Eq. (14) to get

$$\partial_{t2} n = 0, \tag{25}$$

$$\partial_{t2} (n v_\alpha) + \partial_\beta \Pi_{\alpha\beta}^{(1)} = 0, \tag{26}$$

$$\partial_{t2} (n\varepsilon) + \partial_\alpha Q_\alpha^{(1)} + \partial_\alpha v_\beta \Pi_{\alpha\beta}^{(1)} = 0, \tag{27}$$

where $\Pi_{\alpha\beta}^{(1)}$ and $Q_\alpha^{(1)}$ are momentum and heat fluxes, respectively,

$$\Pi_{\alpha\beta}^{(1)} = \left(1 - \frac{\lambda_1}{2\tau}\right) \sum_{pi} e_{pi\alpha} e_{pi\beta} N_{pi}^{(1)}, \tag{28}$$

$$Q_\alpha^{(1)} = \left(1 - \frac{\lambda_2}{2\tau}\right) \frac{1}{2} \sum_{pi} \mathbf{e}_{pi}^2 e_{pi\alpha} N_{pi}^{(1)}. \tag{29}$$

Terms with the nonequilibrium components of the distribution function $N_{pi}^{(1)}$ can be evaluated using the first-order equations. Now since the circulant matrix A_{ij} in Eq. (3) satisfies the eigenvalue relations

$$\sum_i e_{pi\alpha} e_{pi\beta} A_{ij} = \lambda_1 e_{pj\alpha} e_{pj\beta}, \tag{30}$$

$$\sum_i e_{pi}^2 e_{pi\alpha} A_{ij} = \lambda_2 e_{pj}^2 e_{pj\alpha}, \tag{31}$$

$\Pi_{\alpha\beta}^{(1)}$ and $Q_\alpha^{(1)}$ can be determined in terms of the equilibrium distribution functions

$$\Pi_{\alpha\beta}^{(1)} = \left(1 - \frac{\lambda_1}{2\tau}\right) \sum_{pi} e_{pi\alpha} e_{pi\beta} \times \left(-\tau \sum_j A_{ij}^{-1} (\partial_{t1} + e_{pj\gamma}\partial_\gamma) N_{pj}^{\mathrm{eq}} \right), \tag{32}$$

$$Q_\alpha^{(1)} = \left(1 - \frac{\lambda_2}{2\tau}\right) \frac{1}{2} \sum_{pi} e_{pi}^2 e_{pi\alpha} \times \left(-\tau \sum_j A_{ij}^{-1} (\partial_{t1} + e_{pj\beta}\partial_\beta) N_{pj}^{\mathrm{eq}} \right), \tag{33}$$

where A_{ij}^{-1} is the inverse matrix of A_{ij}. When Eqs. (26)–(27) are evaluated and combined with equations of first and second order in ϵ, the desired macroscopic fluid equations are found:

$$\partial_t n + \partial_\alpha (n v_\alpha) = 0, \tag{34}$$

$$\partial_t (n v_\alpha) + \partial_\beta (n v_\alpha v_\beta) = -\partial_\alpha P + \partial_\alpha (\lambda \partial_\gamma v_\gamma) + \partial_\beta [\mu (\partial_\alpha v_\beta + \partial_\beta v_\alpha)], \tag{35}$$

$$\partial_t (n\varepsilon) + \partial_\alpha (n\varepsilon v_\alpha) = -P \partial_\alpha v_\alpha + \partial_\alpha (\kappa \partial_\alpha \varepsilon) + \mu (\partial_\alpha v_\beta + \partial_\beta v_\alpha) \partial_\alpha v_\beta + \lambda (\partial_\beta v_\beta)^2. \tag{36}$$

On identifying the transport coefficients in Eqs. (34)–(36) with the corresponding terms in thermal Navier-Stokes equations, we determine the values of shear viscosity μ and thermal conductivity κ:

$$\mu = n\epsilon \left(\frac{\tau}{\lambda_1} - \frac{1}{2} \right), \tag{37}$$

$$\kappa = 2n\epsilon \left(\frac{\tau}{\lambda_2} - \frac{1}{2} \right). \tag{38}$$

On choosing the relaxation times (at each lattice node)

$$\tau = \left(\frac{\mu_0}{n(\mathbf{x}, t)} + \frac{1}{2} \right), \tag{39}$$

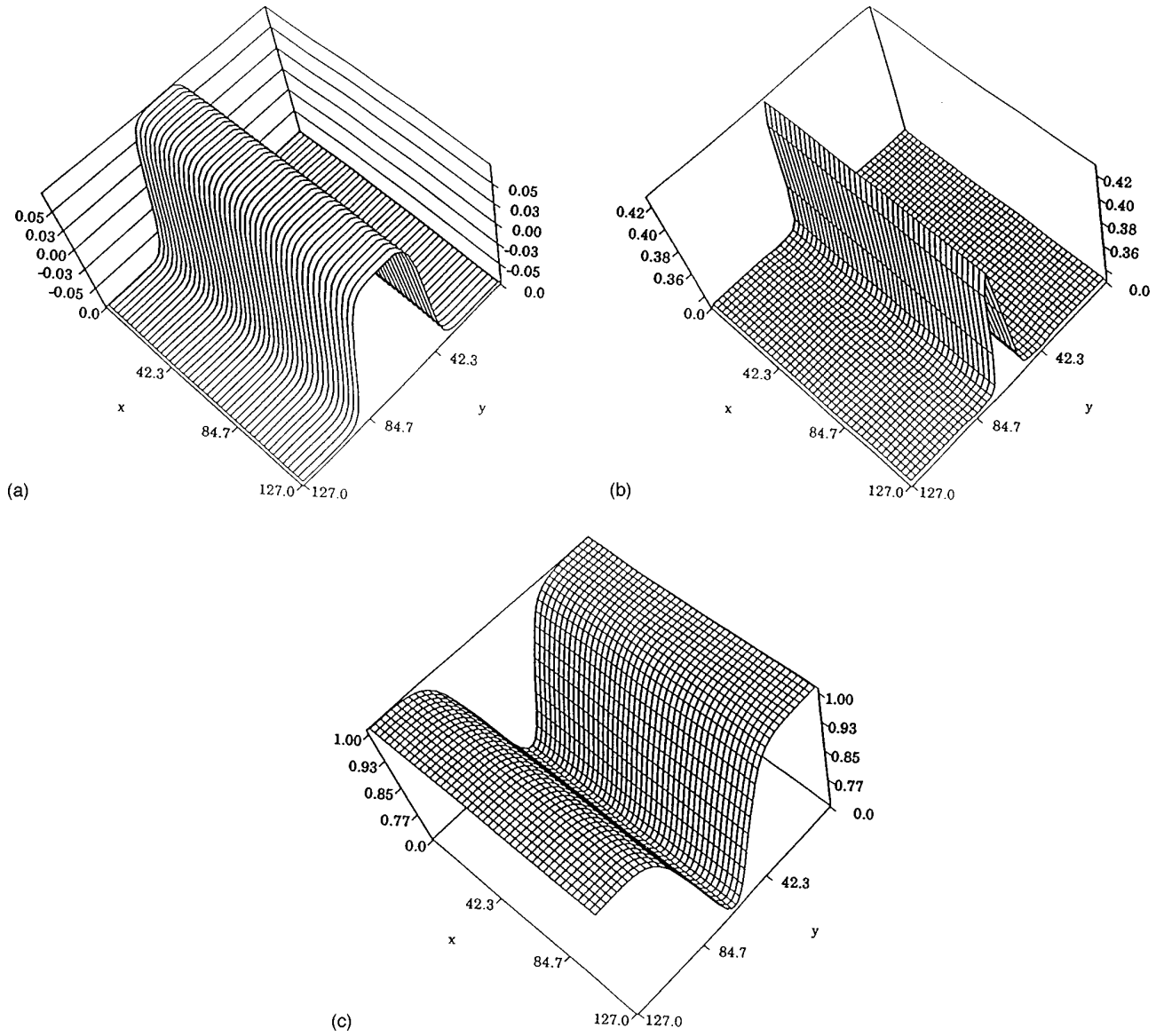

FIG. 1. The unperturbed (a) velocity, (b) temperature, and (c) density profiles. The scale has been normalized to $0 \leqslant x,y \leqslant 127$ for convenience. The hexagonal lattice is 512×512.

$$\theta = \left(\frac{4n(\mathbf{x},t)}{\kappa_0 + n(\mathbf{x},t)} - \frac{2}{\tau} \right), \tag{40}$$

we obtain the final transport coefficients

$$\mu = \mu_0 \varepsilon, \tag{41}$$

$$\kappa = \kappa_0 \varepsilon, \tag{42}$$

where $\kappa_0(\varepsilon)$ is an arbitrary function of the temperature ε, while $\mu_0(\varepsilon) = \alpha \kappa_0(\varepsilon)$ with $\alpha = \text{const}$. The Prandtl number is then

$$\text{Pr} = \frac{\mu_0(\varepsilon)}{\kappa_0(\varepsilon)} = \alpha, \quad \alpha \text{ arbitrary}. \tag{43}$$

Note that the transport coefficients μ and κ are independent of density but are functions of temperature, as is necessary from standard kinetic theory [15]. The above choice of temperature dependence of μ_0 is dictated by gas kinetic theory [15] in which it is shown that the temperature dependences of the transport coefficients are the same. If κ_0 and μ_0 are chosen to be constants (as in the simulations below), then the transport coefficients have a linear dependence on ε. This is the temperature dependence derived in standard kinetic theory [15] for Maxwell molecules.

It should be noted that in the LBE Chapman-Enskog analysis, there are higher order (cubic in the mean velocity) deviation terms that appear in the momentum and energy equations (35)–(36). Their explicit forms are given in Refs. [11, 16]. However, these cubic deviation terms can be shown [11,16] to be negligible for low Mach number flows and since the flows under consideration here have Mach numbers on the order of 0.1, we have neglected them.

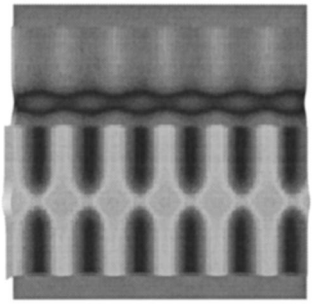

FIG. 2. The initial vorticity (projected onto the x-y plane) after the strong asymmetric perturbation has been applied.

III. SIMULATIONS FOR VARIABLE PRANDTL NUMBER TURBULENT FLOWS

We consider the role of variable Prandtl number on 2D free-decaying turbulence induced by a double velocity shear layer. Simulations are performed on a 512×512 hexagonal grid so that the Reynolds number of this flow Re$\simeq$1655. For simplicity, periodic boundary conditions are imposed, and the plots are renormalized to $0\leqslant x,y\leqslant127$. The unperturbed velocity, temperature, and density profiles are shown in Fig. 1. A strong (40%) asymmetric sinusoidal velocity perturbation is then applied leading to the vorticity profile of Fig. 2. The velocity shear layers (centered at $y=42.3$ and $y=84.7$) will give rise to co- and counter-rotating vortex in their respective layers and the initial 7 vortices in each layer are due to the periodicity in the initial velocity perturbation. Moreover, because of the asymmetric initial perturbation, there is a secondary set of vortices induced (these can be readily seen in Fig. 2. within $10<y<40$ and $45<y<83$).

We shall express the time evolution of the flow in terms of the eddy turnover time, which is related to the TLBE time scale:

$$\frac{T_{\text{eddy}}}{T_{\text{LBE}}}\simeq\frac{L_0}{2\pi v_0}\simeq1020, \tag{44}$$

where $L_0=512$ (length in TLBE units) and v_0 is the unperturbed maximum velocity. To resolve any fine scale structures generated by the turbulence, one requires the dissipation length scale $L_d\geqslant3$ cells (in TLBE units), where

$$L_d\simeq\frac{L_0}{\text{Re}^{1/2}}. \tag{45}$$

In this simulation, $L_d\simeq16$ (since Re=1655), so that all fine scale structures are well resolved.

The evolution of the vorticity profiles for flows with Reynolds number Re=1655 and Prandt number Pr=0.9 is shown in Fig. 3. After one eddy turnover time, $t\simeq1$, the two major vortex layers are being sheared while one sees the beginning of alternating co- and counter-rotating vortices in the regions between the major vortex layers [Fig. 3(a)]. At $t\simeq3$, the imprint of the initial perturbation has been removed by the flow within the two major vortex layers but it still persists within the secondary vortex parings [Fig. 3(b)]. At $t\simeq5$, the vortices within the major layer are beginning to form while the imprint of the initial perturbation on the subsidiary vortices is decaying away [Fig. 3(c)]. By $t\simeq7.5$ [Fig. 3(d)], the two major vortex layers are beginning to interact with each other as the major vortices form. The subsidiary vortices themselves start to merge and have now lost the imprint of the initial perturbation. At $t\simeq10$ [Fig. 3(e)], t

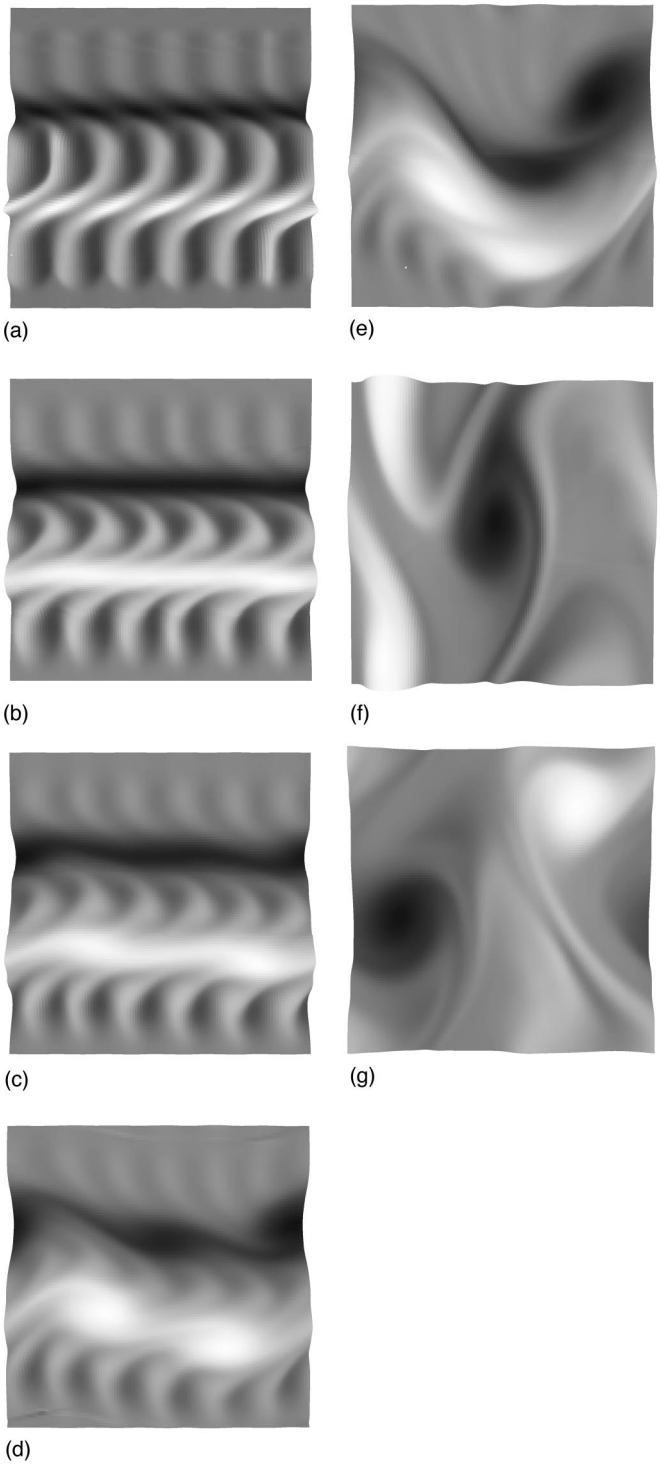

FIG. 3. The evolution of the vorticity for Re=1655 and Pr=0.9 (a) at $t=1000$ LBE time steps (approximately 1 eddy turnover time), (b) at $t=3000$ LBE time steps (3 eddy turnover times), (c) at $t=5000$ LBE time steps (5 eddy turnover times), (d) at $t=7500$ LBE time steps (7.5 eddy turnover times), (e) at $t=10\,000$ LBE time steps (10 eddy turnover times), (f) at $t=15\,000$ LBE time steps (15 eddy turnover times), (g) at $t=20\,000$ LBE time steps (20 eddy turnover times).

$\simeq 15$ [Fig. 3(f)] and $t \simeq 20$ [Fig. 3(g)] eddy turnover times the like-signed vortices merge with the final area being dominated by one co- and one counter-rotating vortex. The vortex merging is, of course, a distinctive property of 2D flows: energy cascades to large scales.

The corresponding decay of the peaked temperature profile is shown for eddy turnover times $t \simeq 1$ [Fig. 4(a)], $t \simeq 5$ [Fig. 4(b)], $t \simeq 7.5$ [Fig. 4(c)], and $t \simeq 10$ [Fig. 4(d)]. At $t \simeq 1$, one clearly sees the imprint of the initial (strong) sinusoidal perturbation on the unperturbed temperature profile, as well as the effect of secondary co- and counter-rotating vortices on the tail of the temperature profile. By $t \simeq 5$, the temperature profile is diffusing and responding to the slight modulating in the major two vortex layers [cf. Fig. 3(c)]. For $t \simeq 7.5$ and $t \simeq 10$, one sees, as expected especially for low Mach number flows, how the flow convection distorts the temperature profile on a faster time scale than diffusive process [cf. vortex layer distortions in Figs. 3(d), and 3(e)].

We now consider the effect on the vorticity and temperature as one increases the Prandtl number to $\mathrm{Pr}=15$ at fixed $\mathrm{Re}=1655$ (by decreasing the conductivity parameter κ_0). We find that there is little effect on the geometry of the dominant vortex structures as projected onto the 2D plane, the differences coming more in the magnitudes. This is shown in Figs. 5(a) and 5(b) for the vorticity at $t \simeq 10$ and 20. What is plotted here is the difference between the vorticity at $\mathrm{Pr}=0.9$ and at $\mathrm{Pr}=15$. At $t \simeq 7.5$, one finds only a maximum vorticity magnitude variation of 3% while at $t \simeq 20$ this magnitude variation can approach 50%. Again, this is to be expected in free-decaying turbulence since the dominant effect comes from convection and not from the transport coefficient terms. This is also seen in the temperature difference profiles, Figs. 6(a)–6(c), for eddy turnover times $t \simeq 1$ (3% maximum difference), $t \simeq 5$ (10% difference), and $t \simeq 10$ (10% difference).

Finally, we shall consider the effect of Reynolds number on the 2D breakup of the double shear layers. For these 512×512 simulations, the eddy turnover time $T_{\mathrm{eddy}} \simeq 1360$LBE time units and $\mathrm{Re}=14\,746$ (Fig. 7) and $\mathrm{Re}=4915$ (Fig. 8). One sees qualitatively the same behavior as before, but occurring at a faster rate for higher Re. At $t \simeq 3.7$, the two major vortex layers are undulating and beginning to break up, with the initial perturbation imprint removed [Figs. 7(a) and 8(a)]. The secondary co- and counter-rotating vorticies can, on close inspection, be seen to be evolving on a faster time scale for $\mathrm{Re}=14\,746$ [Fig. 7(a)] than for $\mathrm{Re}=4915$ [Fig. 8(a)]. By $t \simeq 7.4$, there is now a marked difference in the evolution in the breakup of the major vortex layers and the evolution of these vortices for $\mathrm{Re}=14\,746$ [Fig. 7(b)], $\mathrm{Re}=4915$ [Fig. 8(b)], and $\mathrm{Re}=1655$ [Fig. 3(d)], which is actually at a slightly later time $t \simeq 7.5$ but still has its shear layers themselves somewhat intact. There is a continual difference in the evolution of the space-filling vortices as time evolves [Figs. 7(c) and 8(c) at $t \simeq 12.9$; Fig. 7(d) and 8(d) at $t \simeq 14.8$]. At these higher Reynolds numbers, the evolution of the temperature is considerably different. We find that these profiles are smoothed out by the 2D turbulence within 4 eddy turnover times.

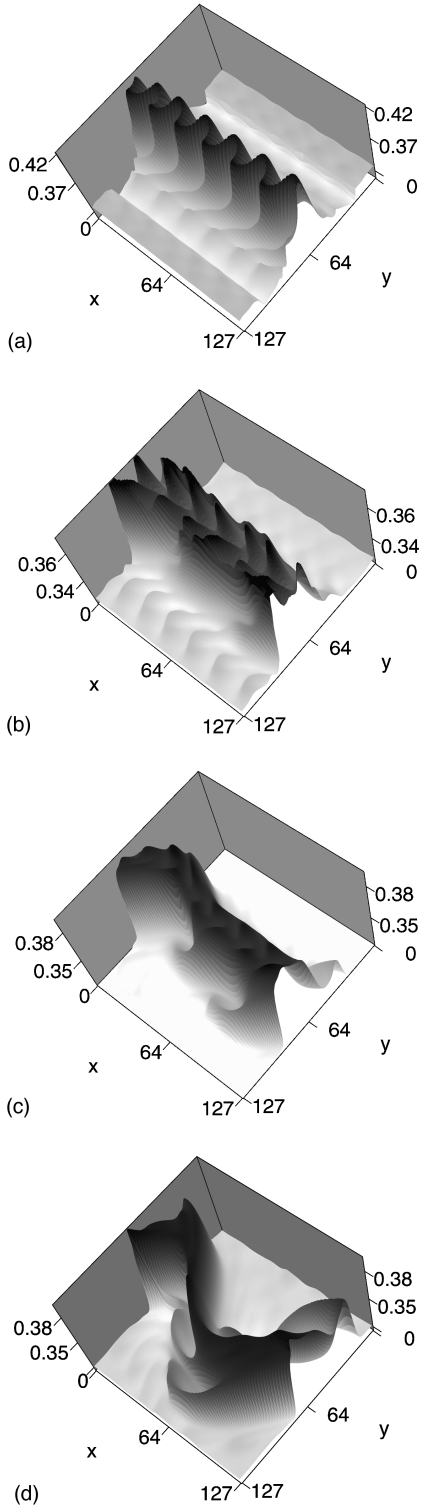

FIG. 4. The evolution of the temperature for $\mathrm{Re}=1655$ and $\mathrm{Pr}=0.9$ (a) at $t=1000$ LBE time units (1 eddy turnover time), (b) at $t=5000$ LBE time units (5 eddy turnover times), (c) at $t=7500$ LBE time units (7.5 eddy turnover times), (d) at $t=10\,000$ LBE time units (10 eddy turnover times).

IV. STABILITY OF TLBE WITH EXTENDED COLLISION OPERATOR

In considering the linear stability of TLBE with extended collision operator [14] the method applied to the stability analysis [17] of the single-time BGK collision operator [19] can be readily applied. In particular, for a uniform global equilibrium with density $n=1$, internal energy $\varepsilon=\varepsilon_0$ and zero mean velocity $\mathbf{v}=0$, the equilibrium distribution function (6) reduces to

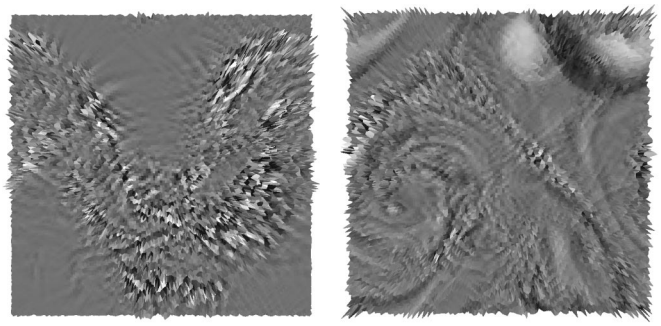

FIG. 5. The evolution of the difference in the vorticity at Re $=1655$—but for different Prandtl numbers: Pr$=15$ and Pr$=0.9$—(a) at $t=10\,000$ LBE time steps (10 eddy turnover times), (b) at $t=20\,000$ LBE time steps (20 eddy turnover times).

$$N_{pi}^{\mathrm{eq}}(\mathbf{x})=A_p(\varepsilon_0)\equiv A_p^{(0)} \tag{46}$$

at any grid point $\mathbf{x}$.

Now apply an initial perturbation $\zeta_{pi}^{(0)}(\mathbf{x})$ to this equilibrium distribution function so that at time $t=0$

$$N_{pi}^{(0)}(\mathbf{x})=A_p+\zeta_{pi}^{(0)}(\mathbf{x}). \tag{47}$$

We use the superscript index to denote the time iteration number.

After free-streaming and extended collisional relaxation at each nodal site, we can determine [17] the new distribution function $N_{pi}^{(1)}(\mathbf{x})$. From this, we deduce that the perturbation at time $t=1$ is given by

$$\begin{aligned}\zeta_{pi}^{(1)}(\mathbf{x})=\sum_{qj}&\left\{\frac{1}{\tau}\left[A_p^0+\left(\frac{e_q^2}{2}-\varepsilon_0\right)A_p'^0+(\mathbf{e}_{pi}\cdot\mathbf{e}_{qj})B_p^0\right]\right.\\&\left.+\left(1-\frac{1}{\tau}\right)\delta_{pq}\delta_{ij}\right\}\zeta_{qj}^{(0)}(\mathbf{x}-\mathbf{e_{qj}})\\&+\sum_{qj}\left[\frac{\theta}{2}\left(B_p^0-\frac{2}{b_pe_p^2}\,\delta_{pq}\right)(\mathbf{e}_{pi}\cdot\mathbf{e}_{qj})\right]\zeta_{qj}^{(0)}(\mathbf{x}-\mathbf{e}_{qj}).\end{aligned} \tag{48}$$

Here the derivative $A_p'^0\equiv A_p'(\varepsilon_0)$ and $B_p^0\equiv B_p(\varepsilon_0)$. The θ term in Eq. (48) arises due to the use of the extended collision operator.

After t iterations, Eq. (48) can be written in matrix form

$$\Xi^{(t+1)}=\mathbf{C}\cdot\mathbf{S}\cdot\Xi^{(t)}, \tag{49}$$

with

$$\Xi_m=\zeta_{pi}(\mathbf{x}_k), \tag{50}$$

where the index k is used for relabeling the lattice nodes for convenience. Also, to write perturbations $\zeta_{pi}(\mathbf{x}_k)$ into a vector Ξ_m, we have introduced an isomorphic map M of indices (p,i,k) into a single index m: i.e., $m=M(p,i,k)$. The collisional relaxation matrix $\mathbf{C}$ has elements

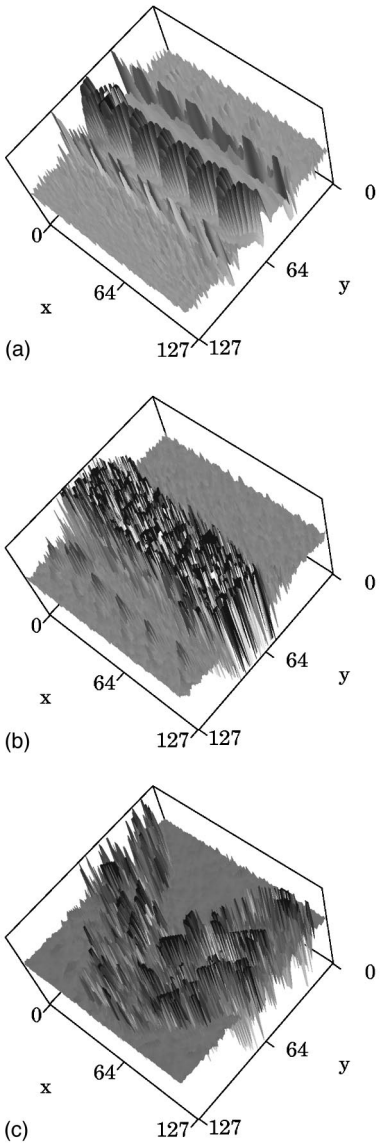

FIG. 6. The evolution of the difference in the temperature at Re$=1655$ but for different Prandtl numbers: Pr$=15$ and Pr$=0.9$; (a) at $t=1000$ LBE time steps (1 eddy turnover time), (b) at $t=5000$ LBE time steps (5 eddy turnover times), (c) at $t=10\,000$ LBE time steps (10 eddy turnover times).

$$\begin{aligned}c_{mn}=&\left\{\frac{1}{\tau}\left[A_p^0+\left(\frac{e_q^2}{2}-\varepsilon_0\right)A_p'^0+(\mathbf{e}_{pi}\cdot\mathbf{e}_{qj})B_p^0\right]\right.\\&\left.+\left(1-\frac{1}{\tau}\right)\delta_{pq}\delta_{ij}\right\}\delta_{kl}+\frac{\theta}{2}\\&\times\left(B_p^0-\frac{2}{b_pe_p^2}\,\delta_{pq}\right)(\mathbf{e}_{pi}\cdot\mathbf{e}_{qj})\,\delta_{kl},\end{aligned} \tag{51}$$

while the streaming matrix $\mathbf{S}$ has elements

$$s_{nm}=\delta_{pq}\delta_{ij}\delta(\mathbf{x}_l-\mathbf{x}_k-\mathbf{e}_{qj}). \tag{52}$$

Here $n=M(q,j,l)$. The dimensionality of the matrix $\mathbf{C}\cdot\mathbf{S}$ (for $L_0=512$) is on the order of $3.4e+06\times3.4e+06$. The matrix $\mathbf{C}\cdot\mathbf{S}$ is real but asymmetric for more than 1 moving speed, as is required for TLBE under any chosen lattice.

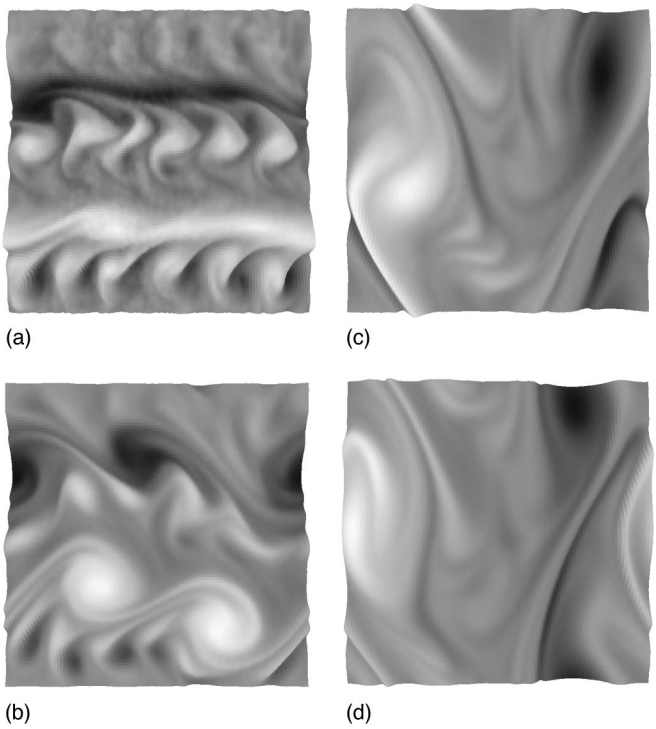

FIG. 7. The evolution of the vorticity for the double shear layer, but now at Re=14 746 and Pr=0.44 on a 512×512 hexagonal grid. (a) At $t=5000$ LBE time steps (3.7 eddy turnover times), (b) at $t=10\,000$ LBE time steps (7.4 eddy turnover times), (c) at $t\simeq 17\,500$ LBE time steps (12.9 eddy turnover times), (d) at $t=20\,000$ LBE time steps (14.8 eddy turnover times).

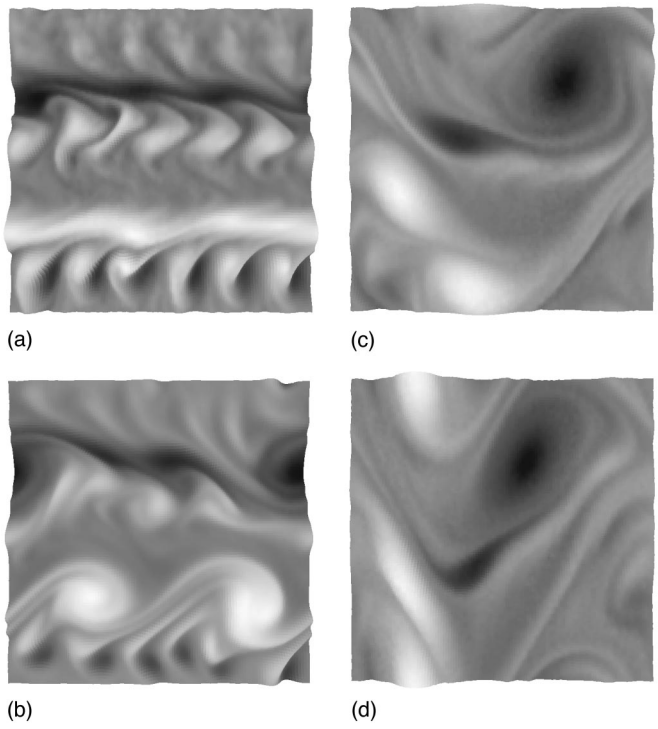

FIG. 8. The corresponding evolution for the vorticity but now at Re=4915 (a) at $t=5000$ LBE time steps (3.7 eddy turnover times), (b) at $t=10\,000$ LBE time steps (7.4 eddy turnover times), (c) at $t\simeq 17\,500$ LBE time steps (12.9 eddy turnover times), (d) at $t=20\,000$ LBE time steps (14.8 eddy turnover times). These runs were actually at Pr=1.32, but as we have already noted, there are no direct effects on the geometric vorticity structures.

Without appealing to the tremendous memory requirement for a matrix of this size, it is impossible to use standard tools, such as NAG library or IDL, for eigenvalue analysis because of the accumulation of numerical errors. However, the form of the matrix $\mathbf{C}\cdot\mathbf{S}$ allows the use of efficient iterative methods.

From the stability point of view, we are interested only in the spectral radius ρ_λ of the matrix $\mathbf{C}\cdot\mathbf{S}$, i.e., the maximum absolute value of all its eigenvalues λ_m. For this purpose, we adopt the method of powers [18]. Suppose that an $M\times M$ matrix $\mathbf{A}$ has M linearly independent eigenvalues $\mathbf{w}_m$ with corresponding eigenvalues λ_m, $m=1,...,M$. An arbitrary vector $\mathbf{v}_0$ can then be expressed as

$$\mathbf{v}_0=\sum_{m=1}^{M}\alpha_m\mathbf{w}_m \tag{53}$$

so that the nth iterated vector $\mathbf{v}_n$,

$$\mathbf{v}_n=\mathbf{A}^n\mathbf{v}_0=\sum_{m=1}^{M}\lambda_m^n\alpha_m\mathbf{w}_m\,. \tag{54}$$

Let λ_1 be the dominant eigenvalue: $|\lambda_1|>|\lambda_m|$, for all $m>1$. Provided $\mathbf{v}_0$ is not orthogonal to $\mathbf{w}_1$ (so that $\alpha_1\neq 0$)

$$\lim_{n\to\infty}\frac{1}{\lambda_1^n}\mathbf{A}^n\cdot\mathbf{v}_0=\alpha_1\mathbf{w}_1 \tag{55}$$

so that

$$\lambda_1=\lim_{n\to\infty}\frac{(\mathbf{y}\cdot\mathbf{v}_{n+1})}{(\mathbf{y}\cdot\mathbf{v}_n)} \tag{56}$$

for any vector $\mathbf{y}$ not orthogonal to $\mathbf{w}_1$. In practice, for the nth approximation of the leading eigenvalue $\lambda_1^{(n)}$, one takes the quotient of the maximum components of two successive vectors $\mathbf{v}_n$ and $\mathbf{v}_{n+1}$.

The convergence to λ_1 in Eq. (56) is guaranteed only if a dominant (single or multiple) real eigenvalues exists. It is easy to derive a similar expression for the case in which a single complex pair of eigenvalues dominates. Strictly speaking, one would have to treat individually all special cases [i.e., all possible combinations of real and complex eigenvalues of the same (maximum) absolute values]. However, this is essentially impossible considering the number of eigenvalues involved. Instead of this, if Eq. (56) fails to converge, we take a long-time geometric average

$$|\lambda_1^{(n)}|=\left[\frac{F_{\max}^{(n)}}{F_{\max}^{(n-I)}}\right]^{1/I}, \tag{57}$$

where

$$F_{\max}^{(n)}\equiv\max[\zeta_{pi}^{(n)}(\mathbf{x}_k)] \tag{58}$$

with suitably chosen span I. In what follows, we refer the value $|\lambda_1|$ as the spectral radius ρ_λ.

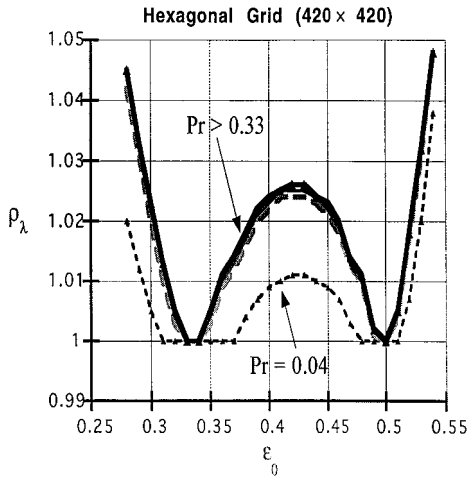

FIG. 9. The spectral radius for a hexagonal 420×420 grid as a function of ε_0 for various Prandtl numbers. We find that the spectral radius becomes independent of the Prandtl number for Pr >0.33 [plotted is the spectral radius for Pr$=0.33$, Pr$=0.5$, Pr $=1.17$, and Pr$=$infinity].

In Figs. 9–11, we plot the spectral radius as a function of initial internal energy ε_0 for various Prandtl numbers. From our work on the numerical stability of TLBE 13-bit hexagonal [9] and square models [20] with single-time BGK relaxation, it was determined that the spectral radius becomes independent of lattice size provided that the hexagonal lattice size was not less than 400×400, and the square lattice was not less than 80×80. In Fig. 9, the spectral radius is plotted at $\tau=0.502$ (i.e., $\mu_0=0.002$) for the hexagonal lattice. Note that for an equilibrium velocity $\mathbf{v}_0=0.08$, this would correspond to a Reynolds number $\geqslant50\,000$. For very low Prandtl numbers, one finds two moderately sized ''stability'' windows in temperature. As the Prandtl number increases, these ''stability'' windows shrink considerably until they become invariant to the Prandtl number for Pr>0.33. The corresponding spectral radius plot for the square lattice is shown in Fig. 10 for $\tau=0.55$ (i.e., $\mu_0=0.05$ and Re on the order of 2000). One can achieve a meaningful stability window at practical Prandtl numbers for the square lattice for $\tau=0.6$ (i.e., $\mu_0=0.1$). Fig. 11.

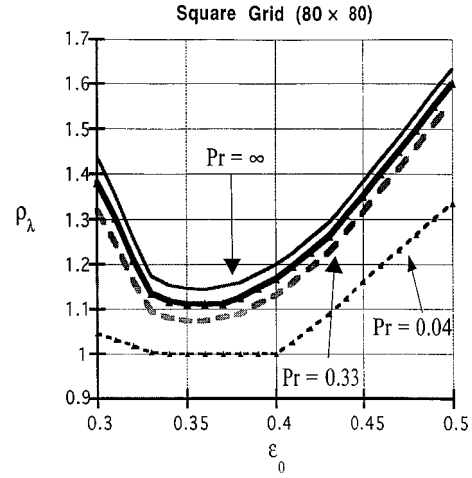

FIG. 10. The spectral radius for the 13-bit TLBE model of Ref. [20] on an 80×80 square grid for various Prandtl numbers: Pr $=0.04$, Pr$=0.33$, Pr$=1.17$ and Pr$=$infinity.

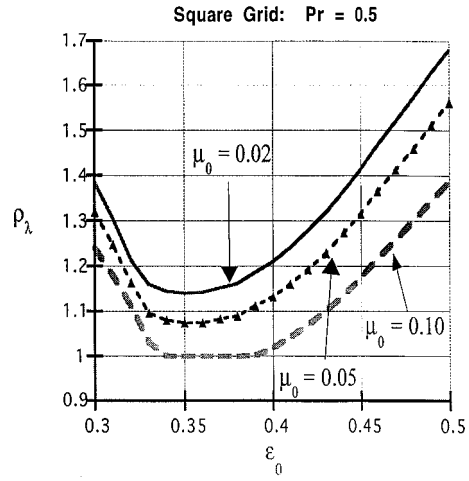

FIG. 11. The spectral radius for the 13-bit TLBE model of Ref. [20] on a 80×80 square grid for various μ_0 at Pr$=0.5$.

V. CONCLUSIONS

To handle flows with variable Prandtl number, we have proposed an extended collision matrix that includes the usual BGK form as a special case. The use of full collision matrix with different eigenvalues was previously attempted by MacNamara and Alder [12]. However, their approach fails to produce the correct transport coefficients and they find that they lose the correct form of the energy conservation equation. A somewhat different approach was proposed by Chen *et al.* [13]. They introduce an additional free parameter into the form of the equilibrium distribution function N_{pi}^{eq}, and use this to have a flexible ratio of viscosity and thermal conductivity. However, incorporation of the additional free parameter produces an unphysical term in the heat flux vector and the minimization of such unphysical effects requires this

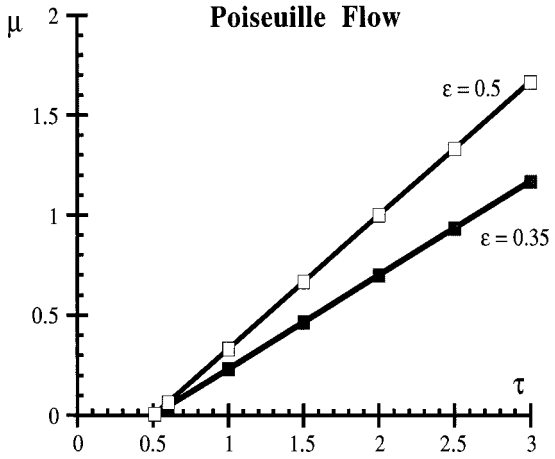

FIG. 12. Shear viscosity μ for isothermal Poiseuille flow as a function of relaxation parameter τ as determined from the extended collision operator TLBE (open squares, dark squares) and from the Chapman-Enskog theory (solid lines) for 2 values of the internal energy $\varepsilon=0.35$ and 0.5. These results were generated at Pr$=0.1$. Table I verifies the well-known result that μ is independent of Pr.

TABLE I. A verification that the TLBE viscosity is independent of Prandtl number in isothermal Poiseuille flow. The mean simulation value and the standard deviation are computed for 50 values of the Prandtl number, $0.1 \leqslant \mathrm{Pr} \leqslant 9.9$. There is also excellent agreement between TLBE-μ and the theoretical Chapman-Enskog μ.

τ	μ (theory)	$\langle \mu$ (simulation)$\rangle$	std. (simulation)
0.51	0.666 67 (-2)	0.682 37 (-2)	2.0 (-9)
0.6	0.666 67 (-1)	0.666 26 (-1)	3.7 (-8)
1.0	0.333 33	0.333 37	4.04 (-6)
1.5	0.666 67	0.666 36	3.18 (-5)
2.0	1.0000	0.998 59	1.07 (-4)
2.5	1.3333	1.3293	2.54 (-4)
3.0	1.6667	1.6583	4.93 (-4)

free parameter value to be close to unity. As a result, their scheme allows Prandtl number variations only within a limited range.

An advantage of the extended collision matrix presented here is that it is simple and computationally efficient. Because of its eigenvalue properties, matrix inversion is as trivial as in the case of scalar BGK operator. Also with the additional free parameter introduced in the off-diagonal components, one now has multi time-scale relaxation parameters that allow generalizations to variable Prandtl number simulations. It is also important to remove the density dependence at each lattice node from the transport coefficients, and this can be readily accomplished.

We have carried out simulations of a 2D free decaying turbulence induced by a strongly perturbed double velocity shear layer. In particular, we have considered the effect of this turbulence at various Prandtl numbers. A linear stability analysis indicates that varying the Prandtl number does not adversely affect the limited stability window in TLBE models invoking free-streaming in its difference scheme. Since we are here dealing with free-decaying turbulence, we find (not unexpectedly) that Prandtl number variation does not have a leading order effect on the geometric structures as they evolve in time—the effects of advection mask the effects of transport. However, we do notice significant magnitude variations in the size of these structures.

ACKNOWLEDGMENTS

This work was supported by DOE and a joint U.S-Czech grant. Some of these vorticity plots (in color) can be viewed at http://physics.wm.edu/~vahala/may97.html

APPENDIX: SOME NUMERICAL TESTS ON THE EXTENDED COLLISION OPERATOR

We now present details of some of the numerical test we have performed to verify that our matrix collision operator on the hexagonal lattice accurately simulates variable Prandtl number flows. In particular, we show for isothermal Poiseuille flow that the TLBE viscosity μ is independent of the Prandtl number and the TLBE thermal conductivity κ (determined from the heat transfer across a linear temperature gradient, using Fourier's law $\mathbf{q} = -\kappa \nabla T$) varies inverses with the Prandtl number. We also find excellent agreement between the TLBE transport coefficients and those determined theoretically from the Chapman-Enskog theory, and for definiteness we scan the Prandtl number range $0.1 \leqslant \mathrm{Pr} \leqslant 9.9$ in steps of 0.2, for each relaxation parameter value τ (here we consider values $\tau = 0.51$, 0.6, 1.0, 1.5, 2.0, 2.5, and 3.0). The boundary conditions are here enforced by standard bounce back.

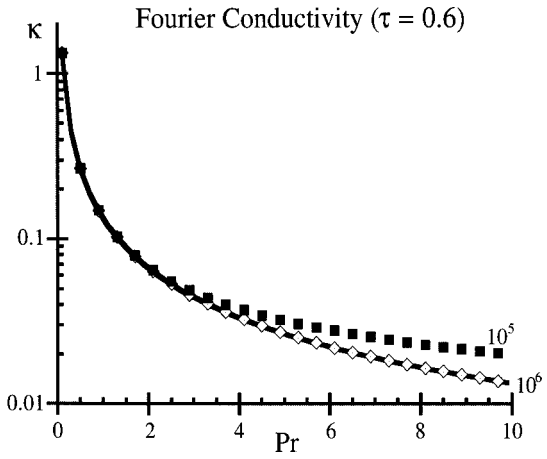

FIG. 13. The dependence of the thermal conductivity κ on the Prandtl number Pr at relaxation parameter $\tau = 0.6$. The Chapman-Enskog theory (solid line) gives $\kappa \approx (\mathrm{Pr})^{-1}$. TLBE simulations indicate that one must perform up to 10^6 TLBE time steps to reach steady state (open diamonds), and one finds excellent agreement with theory. For comparison, the TLBE simulation result after 10^5 iterations are also shown (dark squares). The simulations are performed for 50 Pr values. Table II tabulates the power curve fits for different τ.

1. Poiseuille flow

The viscosity is related [9] to the momentum at the channel center by

$$\mu = \frac{L^2}{8 v_{cn}} f, \tag{A1}$$

where L is the channel width, v_{cn} is the mean velocity at the channel center, and f is the magnitude of the forcing. The

TABLE II. TLBE determination of the dependence of the thermal conductivity κ on the Prandtl number, $0.1 \leqslant \mathrm{Pr} \leqslant 9.9$, using the power-law fit $\kappa = A(\mathrm{Pr})^m$. There is excellent agreement in both parameters A and m between the theoretical Chapman-Enskog κ and the TLBE-κ. Note that for low values of the relaxation parameter τ, one must proceed to more time iterations in order to reach steady state.

τ	A (theory)	A (simulation)	m (theory)	m (simulation)
0.6 (10^5 iter.)	0.13333	0.13726	-1	-0.8829
0.6 (10^6 iter.)	0.13333	0.13405	-1	-0.99996
1.0	0.66667	0.6699	-1	-0.9975
1.5	1.3333	1.3405	-1	-0.99997
2.0	2.0000	2.0107	-1	-1
2.5	2.6667	2.681	-1	-1
3.0	3.3333	3.3512	-1	-1

viscosity μ must be independent of the Prandtl number. In Fig. 12, the Chapman-Enskog viscosity [determined from Eq. (39) and (41)] is plotted as a function of the relaxation time τ and compared to the simulation viscosity determined from Eq. (A1) for two values of the internal energy $\varepsilon=0.5$ and 0.35. We find excellent agreement. In fact, the curve fits (for Prandtl number Pr$=0.1$) are as follows:

$$\varepsilon=0.5: \quad \text{theory:} \quad \mu_{\text{th}}=-0.33333+0.66667\tau,$$

$$\text{simulation:} \quad \mu_{\text{sim}}=-0.33157+0.6648\tau,$$

and

$$\varepsilon=0.35: \quad \text{theory:} \quad \mu_{\text{th}}=-0.23333+0.46667\tau,$$

$$\text{simulation:} \quad \mu_{\text{sim}}=-0.23429+0.46786\tau.$$

To show that the viscosity μ is independent of the Prandtl number, we perform TLBE simulations for these 50 values of Pr in the interval [0.1, 9.9]. For each τ, the results are summarized in Table I in which we give the mean simulation viscosity (averaged over these 50 Prandtl numbers) as well as its standard deviation (''std'' in Table I) and compare them to the Chapman-Enskog viscosity, μ (theory). Our simulations (with $L=128$ and 10^5 time steps in TLBE units) are in excellent agreement with the Chapman-Enskog theory and show conclusively that μ in our TLBE extended collision operator form is independent of the Prandtl number.

2. Fourier heat conduction

The simulation thermal conductivity κ is determined from the Fourier law $\mathbf{q}=-\kappa\nabla T$ by determining the heat transfer across a temperature gradient at zero mean velocity, while the Chapman-Enskog conductivity is determined from Eqs. (38), (40), and (42). Since the channel walls are held at fixed temperatures $\varepsilon=0.5$ and $\varepsilon=0.4999$, the resulting (simulation) temperature profile is linear, leading to a constant temperature gradient ∇T. We immediately note that κ should be inversely proportional to the Pr:

$$\kappa=\frac{A(\tau)}{\text{Pr}} \tag{A2}$$

and hence will give an excellent test for the validity of our extended collision operator. In Fig. 13 we plot the theoretical Chapman-Enskog-κ (solid line) to the simulation-κ for relaxation parameter $\tau=0.6$ for the 50 Prandtl values in the range $0.1\leqslant\text{Pr}\leqslant 9.9$. Because of the low τ, one does not reach a steady state after 10^5 time iterations (dark squares). After 10^6 iterations one reaches steady state and excellent agreement with the Chapman-Enskog κ dependence on $(\text{Pr})^{-1}$. The results of a power-law curve fit for various values of τ are shown in Table II, verifying that our extended TLBE collision operator accurately simulates the $(\text{Pr})^{-1}$ dependence of κ.

[1] U. Frisch, B. Hasslacher, and Y. Pomeau, Phys. Rev. Lett. **56**, 1505 (1986).
[2] S. Wolfram, J. Stat. Phys. **45**, 19 (1987).
[3] U. Frisch, D. d'Humieres, B. Hasslacher, P. Lallemand, and J. Rivet, Complex Syst. **1**, 649 (1987).
[4] F. Higuera and S. Succi, Europhys. Lett. **8**, 517 (1989).
[5] F. Higuera and J. Jimenez, Europhys. Lett. **9**, 663 (1989).
[6] S. Chen, H. Chen, and W. Matteaus, Phys. Rev. Lett. **67**, 3776 (1991).
[7] H. Chen, S. Chen, and W. Matteaus, Phys. Rev. A **45**, R5339 (1992).
[8] Y. H. Qian, D. d'Humieres, and P. Lallemand, Europhys. Lett. **17**, 479 (1992).
[9] F. J. Alexander, S. Chen, and J. D. Sterling, Phys. Rev. E **47**, 2249 (1993).
[10] Y. Chen, H. Ohashi, and M. Akiyama, Phys. Rev. E **50**, 2276 (1994).
[11] Y. Chen, Ph.D thesis, University of Tokyo (1994).
[12] G. McNamara and B. Alder, Physica A **194**, 218 (1993).
[13] Y. Chen, H. Ohashi, and M. Akiyama, Phys. Fluids **7**, 2280 (1995).
[14] H. Chen, C. Teixeira, and K. Molving, Int. J. Mod. Phys. C **8**, 675 (1997).
[15] L. C. Woods, *An Introduction to the Kinetic Theory of Gasses and Plasma* (Oxford University Press, Oxford, 1993).
[16] Y. H. Qian and S. A. Orszag, Europhys. Lett. **21**, 255 (1993).
[17] P. Pavlo, G. Vahala, L. Vahala, and M. Soe (unpublished).
[18] A. Raalston, *A First Course in Numerical Analysis* (McGraw-Hill, New York, 1956).
[19] G. Vahala, P. Pavlo, L. Vahala, and M. Soe, Czech. J. Phys. **46**, 1063 (1996).
[20] Y. H. Qian, J. Sci. Comput. **8**, 231 (1993).